

An Embedded Boundary Approach for Resolving the Contribution of Cable Subsystems to Fully Coupled Fluid-Structure Interaction

Daniel Z. Huang^a, Philip Avery^c, Charbel Farhat^{a,b,c}

^a*Institute for Computational and Mathematical Engineering, Stanford University, Stanford, CA, 94305*

^b*Mechanical Engineering, Stanford University, Stanford, CA, 94305*

^c*Aeronautics and Astronautics, Stanford University, Stanford, CA, 94305*

Abstract

Many engineering systems contain cables as subsystems including suspension lines for parachutes, cables in suspended bridges, risers in offshore platforms, airborne refueling systems, and so on. However, the interactions between fluid and cable subsystems receive little attention in the open literature. This work proposes an embedded surface approach, in which the dynamics of the cable is captured by beam elements typically found in finite element structural models, and the geometry of the cable is represented by an embedded surface. It is built on: master/slave kinematics between beam elements (master), and the embedded surface (slave); a highly accurate algorithm for computing the embedded surface displacement based on the beam displacement; and an energy-conserving method for transferring distributed forces and moments acting on the nodes of the discrete surface to beam elements. Hence, both flow-induced forces on the cable and effect of the structural dynamic response of the cable on the nearby flow are taken into account. Moreover, the proposed model can be easily incorporated in the Eulerian computation framework, which enables handling large deformations of the cable subsystem. Finally, the effectiveness of the proposed model is demonstrated using a model airborne refueling system and a challenging supersonic parachute inflation problem.

1. Introduction

Cables as subsystems appear in a wide range of engineering and scientific applications, such as suspension lines in the parachute dynamics [1, 2, 3, 4, 5, 6, 7], offshore drilling and production risers [8, 9, 10]. and airborne refueling systems [11, 12, 13, 14]. When immersed in the flow, cable structures can be responsible for strong fluid-structure interactions that may significantly affect the performance of the system they are attached to. Their interactions with the fluid flow are significant, which cause drag reduction for the supersonic parachute system due to disturbing the front bow shock, and give rise to the vortex-induced vibration even fatigue damage of offshore systems. Therefore, to model it is important.

In computational fluid dynamics (CFD), the local fluid cable subsystem interactions consist of two parts, flow-induced forces on the cable and effect of the structural dynamic response of the cable on the nearby flow. Several efforts have been made to account it. Strip theory [10, 9], in which computations are conducted on several cross sections, was applied to analyze the vortex-induced vibrations on deepwater risers. One-way coupling is applied in [2], which constructed empirical flow-induced load formulas on the parachute suspension lines depending on the normal velocity and tabulated drag coefficients. The effect of suspension lines on the fluid flow was modeled by adding source terms based on the inertial and elastic forces of the structure in [7, 15]. Besides, the "brute force" approach [8] was able to resolve complex phenomena due to the presence of a cable, however, the computational cost might be challenging, particularly when the size of its cross section is small compared to the characteristic length of the cable subsystem. Moreover, this issue is exacerbated by the fact that from a structural dynamics viewpoint, the geometry of a cable is typically modeled using line elements, which complicates the task of transferring information between its structural and fluid representations. For

Email addresses: zhengyuh@stanford.edu (Daniel Z. Huang), pavery@stanford.edu (Philip Avery), cfarhat@stanford.edu (Charbel Farhat)

body-fitted CFD meshes, a “dressing” approach based on phantom surface elements and massless rigid elements was proposed in [3] to address this issue. While it can also be used in non body-fitted CFD frameworks, this approach has computational disadvantages that are identified and discussed in this work. For this reason, an alternative embedded boundary approach is proposed for computing cable-driven fluid structure interactions. This approach is more robust than the “dressing” approach and is characterized by a superior computational performance. It is based on: master/slave kinematics between the line representing the geometry of a cable typically found in finite element structural models, and a discretization of its true surface that is embedded in the CFD mesh; a highly accurate algorithm for computing the embedded surface displacement based on the beam displacement; and an energy-conserving method for transferring distributed forces and moments acting on the nodes of the discrete surface to the nodes of the discrete line enclosed by that surface.

Another challenge for modeling the fluid cable subsystem interactions is the large deformation, caused by the large length diameter ratio or highly flexibility of these cables. To relieve this issue, embedded or immersed boundary methods (EBMs or IBMs) [16, 17, 18, 19, 20] are used in the present study, which are effective for highly nonlinear Fluid-Structure Interaction (FSI) problems. Both “dressing” approach and embedded boundary approach are incorporated into the in-house Eulerian computational framework FIVER [20, 21, 22, 23]— A Finite Volume method with Exact two-material Riemann Problems. To track the boundary layers around the cable subsystem, adaptive mesh refinement [24] is applied, which enables reasonable mesh resolution near the cable subsystem.

The remainder of the paper is organized as follows. First, the “dressing” approach is introduced in section 2. Then, the embedded surface approach and its properties are discussed in section 3. Next, the embedded framework and governing equations are briefly overviewed in section 4. The performance of the discussed models are assessed in section 5 by comparing their results on a model airborne refueling system and a challenging supersonic parachute inflation problem. Finally, conclusions are offered in section 6.

2. Background: the “dressing” approach

The cable subsystems are generally modeled as one-dimensional beam elements or cable elements, thanks to the large length diameter ratio, but the fluid domain is generally three dimensional. The detection of these one-dimensional elements and defining proper structure normals are ambiguous in this scenario. Hence, it is challenging to capture the local fluid-structure interaction near the cable subsystem. Inspired by the fish-bone aeroelastic models, the “dressing” approach considers a “super” beam element (See fig. 1-left), which consists of the one-dimensional beam elements, massless rigid beam elements, and a massless discrete surface Σ_p . The discrete surface represents the real geometry of the cable, where the fluid-structure interaction happens. Namely, the flow-induced forces are evaluated on this surface, and the effect of the cable on the flow is also enforced here through the transmission boundary conditions. The beam elements and the discrete surface are connected with massless rigid beam elements, which are all coupled and solved together by the structural solver. Besides modeling cable subsystems, thoughts of the equivalent beam element are widely used in simplified models, like very-flexible aircrafts [25, 26] and turbine blades [27, 28].

The “dressing” approach is able to handle the fluid-cable subsystem interaction consistently, and the mesh generating procedure, although tedious, can be automated. However, the mass matrix entries corresponding to the nodes on the dressing surface are zero, due to the massless assumption. This singularity could be an issue for explicit structural integrators, which are needed for highly nonlinear fluid-structure interaction problems, like contact problems or damage mechanics.

3. Alternative embedded boundary approach

The zero mass singularity in the “dressing” approach can be resolved through a matching procedure [29], which is common for handling non-conforming fluid/structure interfaces in aeroelastic computations. In the current scenario, the structure solver solves only the dynamics of the one-dimensional beam elements and the fluid solver sees only the discrete surface Σ_p , which allows evaluating the force load and moment

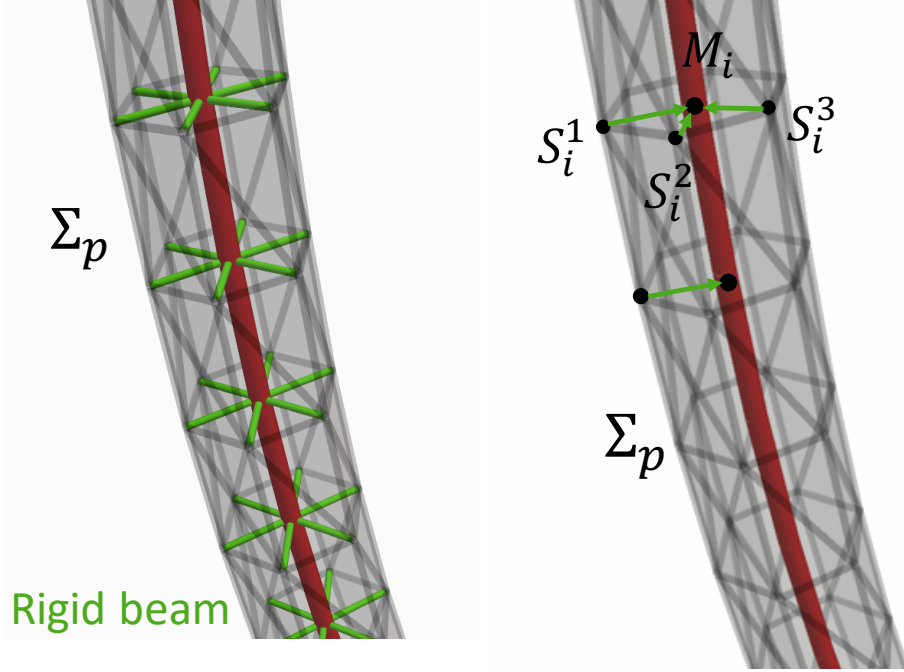


Figure 1: Schematics of a "super" beam element from the "dressing" approach (left) and the "matched" beam from the embedded boundary approach (right). The discrete surface Σ_p , representing the real cable geometry, encloses the one-dimensional beam elements (red). They are connected by the massless rigid beam elements (green) in the "dressing" approach (left).

precisely. To bridge the dynamics of the one-dimensional beam elements and the discrete surface, a master-slave kinematics is applied. The slave surface follows the master beam, and meanwhile the load computed on the slave surface are transferred to the master beam. The detailed load and motion transfer algorithm is as follows:

- Match each slave node S_i^j on the embedded surface with a master point M_i on some beam element using the closest point projection. The superscript j of S_i^j indicates that this matching procedure might be a many-to-one map. The distance vector between these two locations in the initial configuration is denoted by \mathbf{d}_i^j , which is written as

$$\mathbf{x}_{S_i^j}^0 = \mathbf{x}_{M_i}^0 + \mathbf{d}_i^j. \quad (1)$$

- At each time step, the displacement $\mathbf{u}_{S_i^j}$ and velocity $\dot{\mathbf{u}}_{S_i^j}$ of the slave node S_i^j are formulated as

$$\mathbf{u}_{S_i^j} = \mathbf{u}_{M_i} + \mathcal{R}(\boldsymbol{\theta}_{M_i})\mathbf{d}_i^j - \mathbf{d}_i^j \quad \text{and} \quad \dot{\mathbf{u}}_{S_i^j} = \dot{\mathbf{u}}_{M_i} + \dot{\boldsymbol{\theta}}_{M_i} \times \mathcal{R}(\boldsymbol{\theta}_{M_i})\mathbf{d}_i^j, \quad (2)$$

where \mathbf{u}_{M_i} and $\boldsymbol{\theta}_{M_i}$ are displacement and rotation freedoms of the matched beam point, and $\dot{\mathbf{u}}_{M_i}$ and $\dot{\boldsymbol{\theta}}_{M_i}$ are its velocity and angular velocity, respectively. \mathcal{R} is the rotation matrix at the matched beam point, which depends on the rotation freedoms $\boldsymbol{\theta}_{M_i}$.

- Meanwhile, the force \mathbf{f}_{M_i} and moment \mathbf{p}_{M_i} on the master point M_i are induced from the nodal force $\mathbf{f}_{S_i^j}$ of the slave node as follows,

$$\mathbf{f}_{M_i} = \sum_{j=1}^{n_i} \mathbf{f}_{S_i^j} \quad \text{and} \quad \mathbf{p}_{M_i} = \sum_{j=1}^{n_i} \mathcal{R}(\boldsymbol{\theta}_{M_i})\mathbf{d}_i^j \times \mathbf{f}_{S_i^j}, \quad (3)$$

where n_i is the number of slave nodes that are matched to M_i .

The master-slave procedure effectively decouples the freedoms of the slave nodes from the structural solver, hence removes the zero mass singularities from the "dressing" approach and meanwhile accelerates the structural solver. It is worth mentioning that, although decoupled, the aforementioned procedure guarantees conservativity. Consider a virtual displacement field $\delta \mathbf{u}_F$ of the flow on the fluid-structure boundary Σ_p , the virtual work of the fluid traction acting on Σ_p can be written as

$$\begin{aligned} -\delta W^F &= \int_{\Sigma_p} \left(-p \mathbf{n} + \tau_F \mathbf{n} \right) \cdot \delta \mathbf{u}_F d\Sigma_p, \\ &= \sum_{i=1}^{n_M} \sum_{j=1}^{n_i} \mathbf{f}_{S_i^j} \cdot \delta \mathbf{u}_{S_i^j}, \end{aligned} \quad (4)$$

where p and τ_F are the pressure and stress tensor of the flow, \mathbf{n} is the outward normal of Σ_p , and the conservative load transfer algorithms [29] is applied to compute the nodal force $\mathbf{f}_{S_i^j}$ at each slave node. And n_M is the number of master points. Substituting eqs. (2) and (3) into eq. (4) leads to

$$\begin{aligned} -\delta W^F &= \sum_{i=1}^{n_M} \sum_{j=1}^{n_i} \mathbf{f}_{S_i^j} \cdot \left(\delta \mathbf{u}_{M_i} + \delta \boldsymbol{\theta}_{M_i} \times \mathcal{R}(\boldsymbol{\theta}_{M_i}) \mathbf{d}_i^j \right), \\ &= \sum_{i=1}^{n_M} \sum_{j=1}^{n_i} \mathbf{f}_{S_i^j} \cdot \delta \mathbf{u}_{M_i} + \left(\mathcal{R}(\boldsymbol{\theta}_{M_i}) \mathbf{d}_i^j \times \mathbf{f}_{S_i^j} \right) \cdot \delta \boldsymbol{\theta}_{M_i}, \\ &= \sum_{i=1}^{n_M} \mathbf{f}_{M_i} \cdot \delta \mathbf{u}_{M_i} + \mathbf{p}_{M_i} \cdot \delta \boldsymbol{\theta}_{M_i}, \end{aligned} \quad (5)$$

Finally, noting that eq. (5) is the virtual work δW^S of the one-dimensional beam structure, therefore, the energy is conservative in the decoupled master-slave procedure. Moreover, the master-slave kinematics does not require that the matched master point M_i coincides with the beam node, in such case the conservative load transferred algorithm in [29] needs to be applied. Although we focus on cable subsystems with circular cross-sections in the present work, this procedure can also be generalized for more complicated surfaces, like bridges [30], turbine blades and flexible aircrafts.

4. Embedded computational framework

The aforementioned cable-subsystem modeling approaches are incorporated into Embedded or Immersed boundary methods (EBMs or IBMs) [31, 32, 33, 34, 35, 19, 17, 18, 20, 21, 36], which are also known under other names, including fictitious domain methods [37] and Cartesian methods [38, 32]. Since they effectively handle FSI applications featured with large structural displacements, rotations, deformations, and/or topological changes [39, 20, 40], and cable subsystems characterized by large length diameter ratio, generally undergo large deformations. Though the arbitrary Eulerian-Lagrangian (ALE) method [41, 42], incorporated with mesh motion algorithms or remeshing techniques [30, 10, 8], has also been applied to explore cable system dynamics. In the present work, we focus mainly on the Eulerian framework, but the cable-subsystem modeling approaches discussed above can straightforwardly be incorporated into the ALE framework, for problems with moderate displacements.

4.1. Governing equation

Let Ω^f denote the fixed fluid domain in the Eulerian computational framework, the conservative form of the Navier-Stokes equations can be written with Einstein notation as

$$\begin{aligned}\frac{\partial \rho}{\partial t} + \frac{\partial \rho v_j}{\partial x_j} &= 0, \\ \frac{\partial \rho v_i}{\partial t} + \frac{\partial \rho v_i v_j}{\partial x_j} + \frac{\partial p}{\partial x_i} &= \frac{\partial \tau_{ij}}{\partial x_j}, \\ \frac{\partial E}{\partial t} + \frac{\partial (E + p)v_j}{\partial x_j} &= -\frac{\partial q_j}{\partial x_j} + \frac{\partial \tau_{ij} v_i}{\partial x_j},\end{aligned}\tag{6}$$

here ρ is the density, $\mathbf{v} = (v_1, v_2, v_3)$ is the velocity vector, p is the pressure, and $E = \rho(e + v_i v_i/2)$ is the total energy per unit volume, where e is the specific internal energy. The viscous stress tensor τ_{ij} and heat flux vector q_i are defined as

$$\tau_{ij} = \mu \left(\frac{\partial v_i}{\partial x_j} + \frac{\partial v_j}{\partial x_i} - \frac{2}{3} \frac{\partial v_k}{\partial x_k} \delta_{ij} \right) \quad \text{and} \quad q_i = -\kappa \frac{\partial T}{\partial x_i},$$

where μ is the dynamic viscosity, δ_{ij} is the Kronecker delta, κ is the thermal conductivity, and T is the temperature of the gas. The system of equations 6 is closed by assuming that the gas is ideal and calorically perfect,

$$p = \rho RT \quad \text{and} \quad e = \frac{R}{\gamma - 1} T,$$

where R and γ are the gas constant and the specific heat ratio.

The governing equations of the dynamic equilibrium of the structure, including the cable-subsystem, are written in a Lagrangian formulation with Einstein notation

$$\rho_o^s \frac{\partial^2 u_i}{\partial t^2} = \frac{\partial F_{im} S_{mj}}{\partial X_j} + \rho_o^s b_i \quad \text{in } \Omega_0^s,\tag{7}$$

where Ω_0^s denotes the initial configuration with the material coordinate X_i . ρ_o^s denotes the structural material density, u_i denotes its displacement vector, F_{ij} denotes the deformation gradient tensor, S_{ij} denotes the second Piola-Kirchhoff stress tensor, and b_i is the vector of body forces acting on Ω_0^s . Given a structural material of interest, the closure of eq. (7) is performed by specifying a constitutive law that relates the second Piola-Kirchhoff stress tensor to the Green symmetric strain tensor

$$E = \frac{1}{2}(F^T F - 1).$$

Dirichlet and/or Neumann boundary conditions are applied to the Dirichlet and Neumann part of the boundary of Ω_0^s , as required by the problem of interest.

In addition to eq. (6), eq. (7) and their associated boundary conditions, the FSI problem resulting from the embedding of the structural system in Ω^f is governed by the transmission conditions

$$v_i = \dot{u}_i \quad \text{on } \Sigma_p,\tag{8}$$

and

$$-p\mathbf{n} + \tau_F \mathbf{n} = J^{-1} F S F^T \mathbf{n} \quad \text{on } \Sigma_p,\tag{9}$$

where \mathbf{n} is the outward unit normal to the deformed configuration of the material interface Σ_p , and $J = \det(F)$. Since the fluid is assumed to be viscous, additional boundary conditions are specified on Σ_p : these are the adiabatic or isothermal boundary conditions, and the appropriate boundary conditions for the turbulence model equations when these are presented.

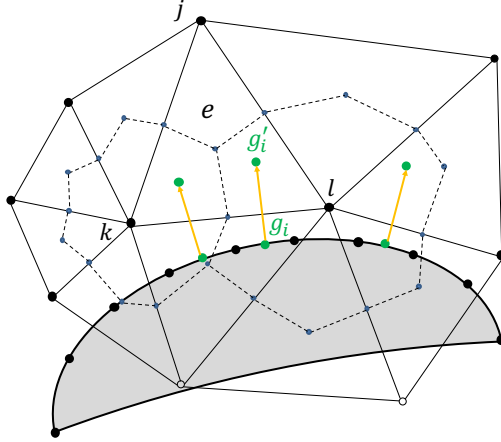


Figure 2: Evaluation of force loads on Σ_p . g_i and g'_i are the Gauss point and the shifted Gauss point associated to a structure boundary or fluid structure interface element.

4.2. Imposition of the transmission condition

Imposition of transmission conditions eqs. (8) and (9) in the Eulerian computational framework is the key factor, which distinguishes one embedded boundary method from another. This paper focus on the in-house Eulerian computational framework—The Finite Volume method with Exact two-material Riemann Problems (FIVER) [20, 43, 22, 23]. This framework has been extensively verified and validated for complex multi-material problems, including FSI problems with large deformations [44], turbulent flows [21], or dynamic fractures [45].

4.2.1. No-slip boundary condition

The no-slip boundary condition eq. (8) embodies the structure to the fluid coupling, i.e. the effect of the structure on the fluid. Its implementation in FIVER consists of two parts: the treatments for the inviscid flux and the viscous flux near the fluid structure interface. For the inviscid flux, a local fluid-structure Riemann problem is formulated and solved at the fluid structure interface [20], which guarantees the characteristic theory and captures well the shock wave or rarefaction wave near the interface. And for the viscous flux, the ghost node method [46, 21] is applied.

4.2.2. Load computation

The force equilibrium condition eq. (9) embodies the fluid to the structure coupling, i.e. the effect of the flow on the structure. The flow-induced load on the embedded surface is generally evaluated first on each Gauss quadrature point g_i of surface elements (See fig. 2). And then, these forces are assembled to the nodal forces. However, the Gauss quadrature point g_i is generally in fluid primal cells that contain inactive nodes. Therefore, to obtain the flow-induced load requires extrapolation, which produces oscillations. Inspired by procedures in [23], modifications are proposed to avoid oscillations in these quantities. The shifted Gaussian points are introduced by shifting each Gaussian point g_i in the direction of the outward normal \mathbf{n} to the wall, to the point g'_i (See fig. 2) defined by

$$g'_i = g_i + h\mathbf{n} \quad (10)$$

where h is the characteristic mesh size of the fluid primal cell containing the Gauss point g_i . And the shifted Gaussian point g'_i is generally in a primal cell, consists of only active nodes.

The pressure force is computed based on the value on the shifted Gaussian point

$$p(g_i) = p(g'_i) + O(h^2), \quad (11)$$

here the $O(h^2)$ term is derived from the Taylor expansion of the pressure field at g_i and the fact $\frac{\partial p(g_i)}{\partial \mathbf{n}} \approx 0$, obtained from the wall normal momentum conservation equation. The pressure at the shifted Gaussian

point g'_i is obtained by *interpolation* in the fluid primal cell containing it. As for the shear force, the shear stress tensor depends on the velocity gradient, which is written in the local coordinate (x'_1, x'_2, x'_3) with x'_3 corresponding to the wall normal direction and x'_1 and x'_2 corresponding to the other two tangential directions, as follows

$$\nabla_{x'} \mathbf{v}(g_i) = \left(\frac{\partial \mathbf{v}}{\partial x'_1}, \frac{\partial \mathbf{v}}{\partial x'_2}, \frac{\partial \mathbf{v}}{\partial x'_3} \right). \quad (12)$$

The components corresponding to the derivatives in the tangential directions are computed based on the finite element approximation

$$\frac{\partial \mathbf{v}(g_i)}{\partial x'_\alpha} \approx \frac{\partial \mathbf{v}(g'_i)}{\partial x'_\alpha} = \sum_{k \in e} \mathbf{v}_k \frac{\partial \phi_k}{\partial x'_\alpha} \quad \alpha = 1, 2 \quad (13)$$

where e is the primal cell that contains the shifted Gauss point, and ϕ_k is the standard piecewise linear test function associated with each fluid node k . The wall normal derivative, which is generally dominant, is approximated directly

$$\frac{\partial \mathbf{v}(g_i)}{\partial x'_3} = \frac{\mathbf{v}(g'_i) - \dot{\mathbf{u}}(g_i)}{h} \quad (14)$$

where $\dot{\mathbf{u}}(g_i)$ is the structure velocity at g_i . When it is necessary, the wall normal derivative can be replaced by the wall model results. The evaluation of the velocity gradients also requires only *interpolations*.

5. Applications

5.1. Airborne refueling system

The first problem considered here is a model problem from airborne refueling systems [12, 13, 14], which is designed to compare the aforementioned "dressing" approach and embedded boundary approach for modeling the cable system. A flexible hose that trails from the tanker aircraft is considered. Its setup is graphically depicted in fig. 3. The computational domain is a cube of size $6\text{m} \times 4\text{m} \times 10\text{m}$. The flexible hose is of length 8m , and its length diameter ratio is $L/D = 119.4$. The top end is pinned, i.e. all six freedoms are fixed, and the other end is free. Therefore, the flexible hose is supposed to undergo large deformations, when interacting with high speed flows, which motivates the usage of Eulerian computational framework, instead of arbitrary Lagrangian Eulerian framework. The detailed parameters of the hose material are listed in table 1. The inflow conditions match the earth atmosphere of 8 km height, which is also listed in table 1.

The hose is discretized by 100 beam elements, and its circular cross section is represented by a hexagon shape. And the "dressing" geometry and embedded boundary surface are discretized by 1200 triangular elements. The fluid domain is discretized by 67686 tetrahedra (initial mesh). To resolve the hose geometry, boundary layer and vortices with the large deformation, the fluid mesh is adaptively refined and coarsened by the newest vertex bisection algorithm [47, 24]. The distance-based and Hessian-based mesh adaptation criteria are applied for boundary layer refinement and vortex refinement separately. The characteristics mesh size near the hose is about 4×10^{-3} m, roughly 1/20 of the diameter. The vortices are tracked by the Hessian of the velocity magnitude with a minimum edge length 1.5×10^{-2} m.

The viscosity of air is modeled using Sutherland's viscosity law, which is $\mu = \mu_0 \sqrt{T}/(1 + T_0/T)$ with $\mu_0 = 1.458 \times 10^{-6}$ kg m⁻¹s⁻¹ and $T_0 = 110.6$ K. The Reynolds number based on the hose diameter is about 3.9×10^5 . Hence, the flow is assumed to have transitioned to the turbulent regime, which is modeled here using the SA turbulence model [48]. Time discretization of the FSI problem is performed using the second-order, time-accurate, implicit-implicit fluid-structure staggered solution procedure developed in the work of [39], and the fluid-structure coupling time-step is $\Delta t_{F/S} = 2 \times 10^{-6}$ s. These FSI simulations start from the same quasi-steady fluid state obtained from a simulation with a fixed rigid structure. The simulation

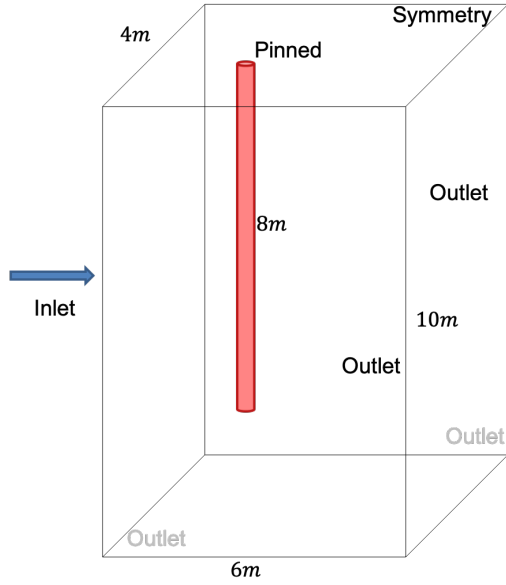


Figure 3: Airbone refueling system: problem setup.

Parameter	Description	Value
L	Length	8 m
ρ_s	Mass of unit length	0.38 kg m^{-1}
D_{out}	Outer diameter	0.067 m
D_{in}	Inner diameter	0.051 m
E	Young's modulus	17 MPa
ν	Poisson's ratio	0.42
H	Altitude	8 km
ρ_∞	Density	0.58 kg m^{-3}
p_∞	Pressure	40000 Pa
T_∞	Temperature	240 K
Ma_∞	Mach	0.5

Table 1: Airborne refueling system: material properties of the hose [12, 14] and the inflow conditions.

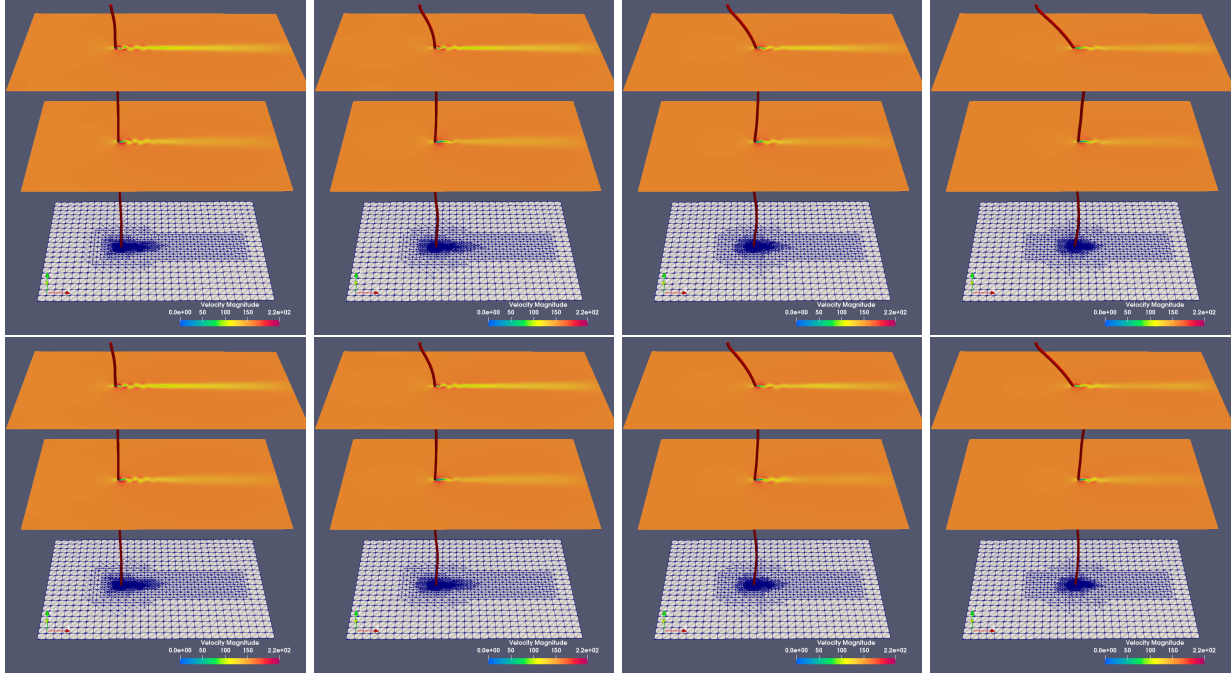


Figure 4: Airborne refueling system: snapshots of the velocity magnitude field computed using the "dressing" approach (top) and the embedded boundary approach (bottom): $t = 0.01s$, $t = 0.02s$, $t = 0.03s$, and $t = 0.04s$ (left to right).

time is $[0, 0.04]s$. Figure 4 graphically depicts the time evolution of the adapted fluid mesh, the velocity magnitude of the fluid flow, and the hose displacement.

The hose is drifted by the high-speed flow, and meanwhile interacts with the vortices behind. The AMR well tracks the boundary layer and the flow features. And it is worth mentioning that both "dressing" approach and embedded boundary approach deliver almost the same flow features and structure displacement fields. The time histories of the drag force on the hose due to the fluid load and the x-displacements of the bottom node and the middle node obtained by both approaches are reported in fig. 5. Great agreements are achieved by both approaches.

5.2. Supersonic parachute inflation dynamics

Next, the inflation dynamics of a Disk-Gap-Band (DGB) parachute in the low-density, low-pressure supersonic Mars atmosphere is simulated [49, 50, 4]. Its main purpose is to understand the effects of the suspension line subsystem on the parachute performance during the deceleration process.

The DGB parachute system (See fig. 6a), which has successfully landed Curiosity Rover on the Mars, contains three main components: the canopy, which is made of F-111 nylon, the suspension lines, which are made of Technora T221 braided cords, and the reentry vehicle [49]. Material properties and geometric parameters of the parachute system are listed in table 2. The simulation starts from the line stretch stage with a folded parachute (See fig. 6b), an idealized analytical representation of the line stretch configuration and the corresponding prestress are employed for the structure initial state. The supersonic flow is incoming at $Ma_\infty = 1.8$, $\rho_\infty = 0.0067 \text{ kg m}^{-3}$ and $p_\infty = 260 \text{ Pa}$. Note that the specified free-stream density and pressure conditions are similar to those observed in the standard Martian atmosphere.

Since the Martian atmosphere is mainly composed of carbon dioxide, the viscosity of this gas is modeled using Sutherland's viscosity law – that is, $\mu = \mu_0 \sqrt{T}/(1 + T_0/T)$ – with $\mu_0 = 1.57 \times 10^{-6} \text{ kg m}^{-1}\text{s}^{-1}$ and $T_0 = 240 \text{ K}$. The Reynolds number based on the canopy diameter is 4.06×10^6 . Hence, the flow is assumed to have transitioned to the turbulent regime, which is modeled here using the Vreman turbulence model [52], with model constant $C_s = 0.07$. The embedding computational fluid domain of size $200\text{m} \times 160\text{m} \times 160\text{m}$

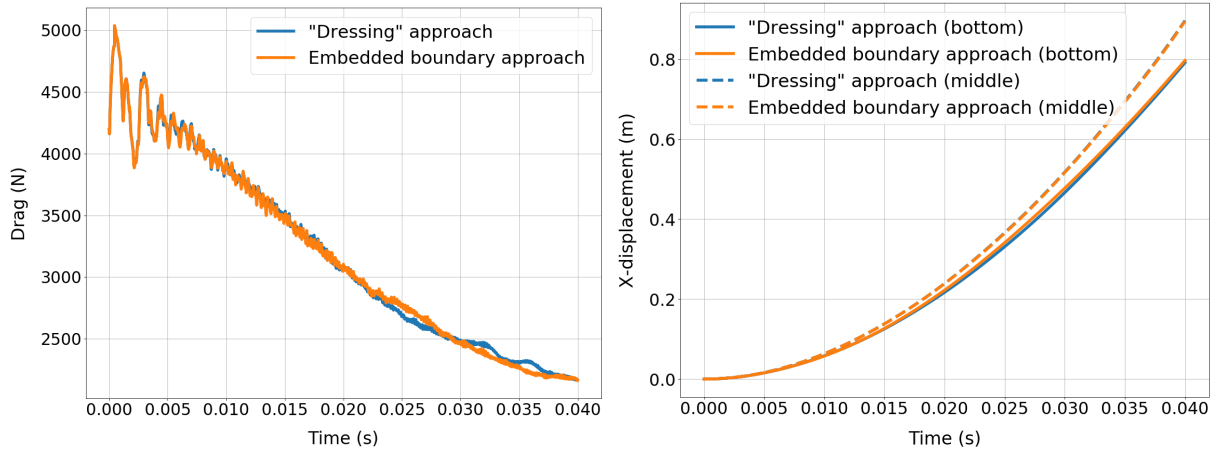


Figure 5: Drag histories (left) and x-displacements (right) on the bottom nodes and middle nodes of the airborne refueling hose predicted by the "dressing" approach (blue) and the embedded boundary approach (yellow).

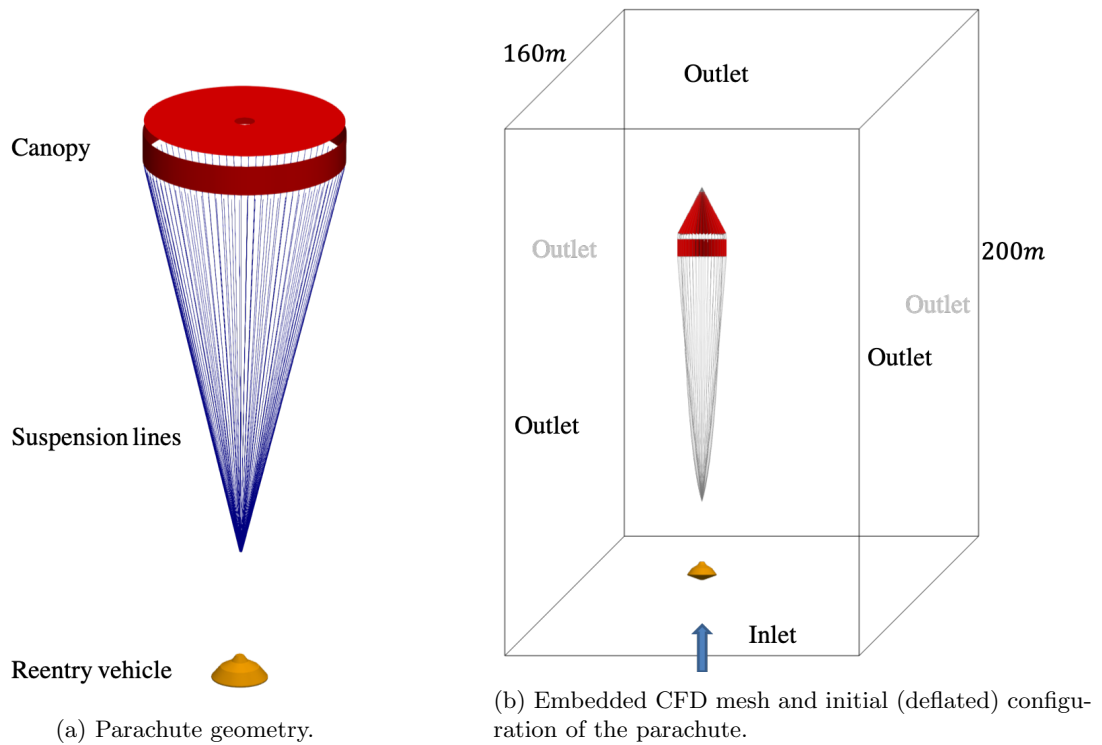


Figure 6: Supersonic parachute inflation dynamics: problem setup.

Component	Properties
Canopy	Diameter = 15.447 <i>m</i> Thickness = 7.607×10^{-5} <i>m</i> $E = 0.945$ <i>GPa</i> $\nu = 0.4$ $\rho = 1154.25$ <i>kg/m</i> ³ Porosity = 0.08
Suspension lines	Length = 36.56 <i>m</i> Diameter = 3.175×10^{-3} <i>m</i> $E = 29.5$ <i>GPa</i> Density = 1154.25 <i>kg/m</i> ³

Table 2: Geometrical and material properties of the parachute [51, 49].

is initially discretized by a mesh composed of Kuhn simplices [47, 24]. Specifically, this initial tetrahedral mesh contains 2778867 vertices and 16308672 tetrahedra. Adaptive mesh refinement (AMR) [53, 47, 24] is applied to track the boundary layer and the flow feature, the characteristic mesh sizes near the reentry vehicle, suspension lines and the canopy are 2.5 cm, 3 mm, and 5 cm, respectively, and the size in the wake regime or near the shock is 10 cm. The canopy of the DGB parachute consists of band gores and disk gores. These are discretized here by 279025 geometrically nonlinear thin-shell ANDES elements [54] (although the membrane stiffness of the fabric is significantly larger than its bending stiffness, both stiffnesses are considered here). The canopy is made of F-111 nylon with 8% void fraction, and the permeability is modeled by the homogenized porous wall model proposed in [55]. There are 80 suspension lines, and each of them is discretized by 500 geometrically nonlinear beam elements. And the reentry vehicle is treated as a fixed rigid body, which is unseen from the structure model. Due to the massive contact of the parachute during its inflation, the explicit central difference scheme is applied for the time discretization of the structure solver, therefore only the embedded surface approach in section 3 is capable of modeling the fluid suspension line subsystem interactions. The cross-section geometry of suspension lines is assumed to be circle with radius $r = 1.6$ mm and represented as the hexagon.

First, the parachute configured in its initial position shown in fig. 6b is assumed to be rigid and the quasi steady-state solution at $T = 0.15$ s is computed (See fig. 7-a). Next, the fluid state is initialized using this quasi steady-state flow solution, the deformable structure is initialized using its initial state described above, and the FSI problem associated with the inflation of the DGB parachute is simulated in the time interval $[0, 0.8]$ s, during which the inflation process is expected to have completed and several breath cycles are captured. Time discretization of the FSI problem is performed using the second-order, time-accurate, implicit-explicit fluid-structure staggered solution procedure developed in the work of [39] and the fluid-structure coupling time-step is roughly $\Delta t_{F/S} = 10^{-5}$ s.

Figures 7 graphically depict the time evolution of the parachute and the flow Mach number field. The bow shock in the front of the canopy, disturbed by the wake generated by the reentry vehicle, vibrates along with the breath cycles of the canopy. Jet-like flow, ejected through the canopy vent and gaps between the band/disk gores, interact with the turbulent wakes behind the canopy. The parachute is fully inflated at $t = 0.23$ s, and it starts breathing after that time.

Although the suspension lines are very thin, they increase geometric blockage in the front of the canopy region, which slightly reduces the flow speed. Moreover, in the interactions with flows, these suspension lines can generate shocks (See fig. 7-e) that alter the wake behind the reentry vehicle, and even disrupt the bow-shock, which agrees with the observations in [5] from sub-scale parachute inflation experiments.

The time-histories of the drag force computed by post-processing the FSI simulation results is plotted in fig. 8. Moreover, drag performance of a simulation without considering the effect of the suspension lines is also presented. The drag force on the suspension lines is negligible, roughly 1%, however, the shocks from the suspension lines create disturbances ahead of the canopy which in turn disrupt the parachute bow-shock,

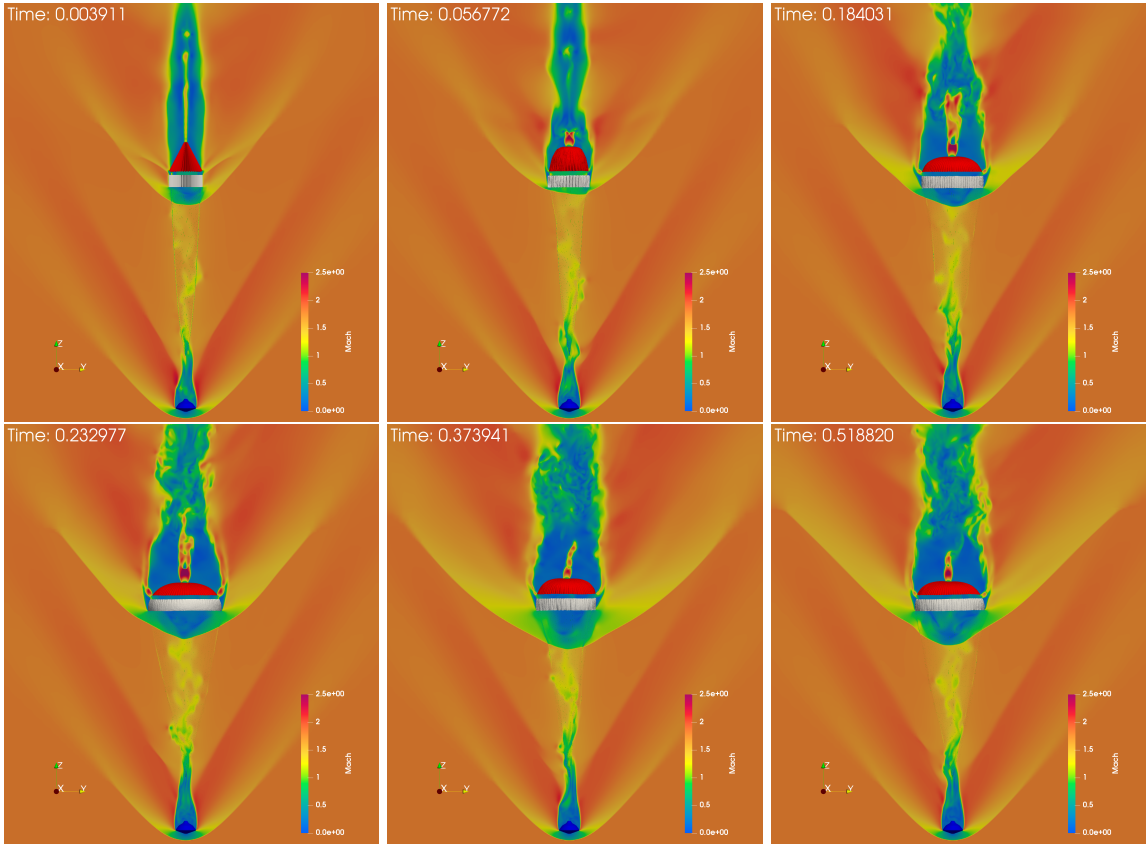


Figure 7: Time-evolution of the parachute and the flow Mach number.

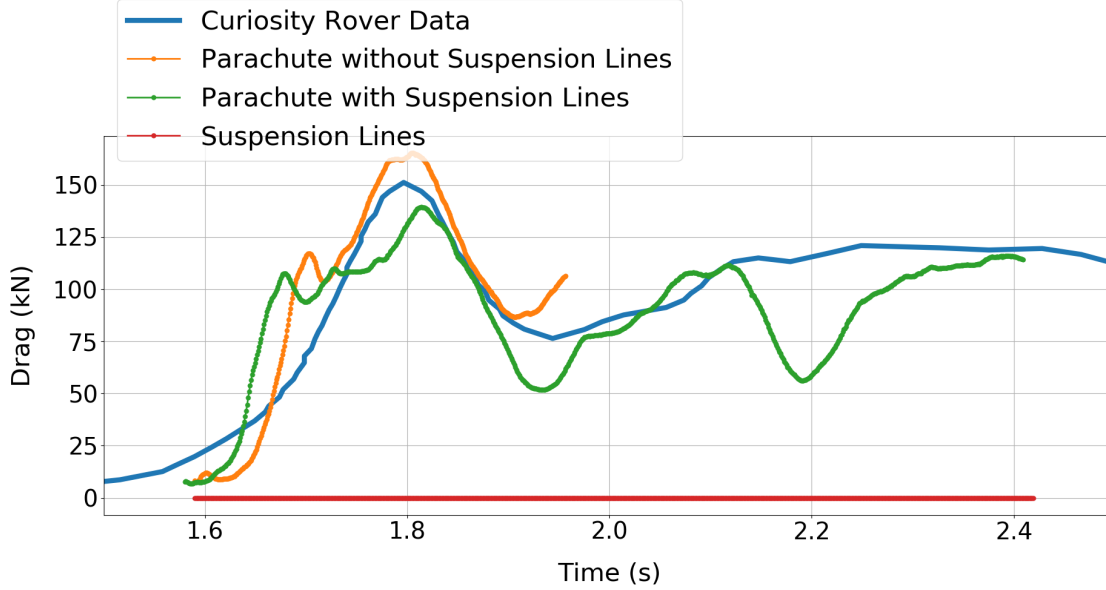


Figure 8: Drag histories of the supersonic parachute inflation dynamics problem: curiosity rover data [49] (blue bold line), simulation with suspension line fluid interaction (orange), simulation with suspension line fluid interaction (green), suspension lines (red)

mix the high pressure and low pressure flows, and reduce the drag force. The drag force data [49] collected from the Curiosity Rover during its Mars landing is also presented in fig. 8. The peak drag prediction, which is related to the material failure, is in good agreement with the landing data, and the relative error is less than 10%.

6. Conclusions

In this paper, we have proposed a simple and practical embedded surface approach to model the fluid cable subsystem interactions in engineering systems. This approach is based on master/slave kinematics with the master beam elements and a slave embedded surface, which represents its real geometry. The fluid solver sees only the slave embedded surface which is used to evaluate the load, while the structure solver sees only the master beam elements. Moreover, it is suitable for Eulerian computational framework. Hence, combining with adaptive mesh refinement techniques, the approach effectively handles large deformations of the cable subsystem. Its application to the simulation of a model airborne refueling system and a challenging supersonic parachute inflation problem has clearly demonstrated its practicality and reasonable computational efficiency. An interesting area for future work would be to extend current model for under-resolved slender structures, like turbine blades and fuselage.

Acknowledgments

Daniel Z. Huang, Philip Avery, and Charbel Farhat acknowledge partial support by the Jet Propulsion Laboratory (JPL) under Contract JPL-RSA No. 1590208, and partial support by the National Aeronautics and Space Administration (NASA) under Early Stage Innovations (ESI) Grant NASA-NNX17AD02G. Daniel Z. Huang thanks Kvamsdal Trond for helpful discussions.

References

- [1] Yuxin Fan and Jian Xia. Simulation of 3d parachute fluid–structure interaction based on nonlinear finite element method and preconditioning finite volume method. *chinese Journal of Aeronautics*, 27(6):1373–1383, 2014.
- [2] Tayfun E Tezduyar, Kenji Takizawa, Creighton Moorman, Samuel Wright, and Jason Christopher. Space–time finite element computation of complex fluid–structure interactions. *International Journal for Numerical Methods in Fluids*, 64(10-12):1201–1218, 2010.
- [3] Zhengyu Huang, Philip Avery, Charbel Farhat, Jason Rabinovitch, Armen Derkevorkian, and Lee D Peterson. Simulation of parachute inflation dynamics using an eulerian computational framework for fluid-structure interfaces evolving in high-speed turbulent flows. In *2018 AIAA Aerospace Sciences Meeting*, page 1540, 2018.
- [4] Jason Rabinovitch, Daniel Z Huang, Raunak Borker, Philip Avery, Charbel Farhat, Armen Derkevorkian, and Lee Peterson. Towards a validated fsi computational framework for supersonic parachute deployments. In *AIAA Aviation 2019 Forum*, page 3275, 2019.
- [5] Anita Sengupta, Richard Kelsch, James Roeder, Mark Wernet, Allen Witkowski, and Mike Kandis. Supersonic performance of disk-gap-band parachutes constrained to a 0-degree trim angle. *Journal of Spacecraft and Rockets*, 46(6):1155–1163, 2009.
- [6] Xinglong Gao, Qingbin Zhang, and Qiangang Tang. Numerical modelling of mars supersonic disk-gap-band parachute inflation. *Advances in Space Research*, 57(11):2259–2272, 2016.
- [7] Yongsam Kim and Charles S Peskin. 3-d parachute simulation by the immersed boundary method. *Computers & Fluids*, 38(6):1080–1090, 2009.
- [8] Rajeev K Jaiman, Farzin Shakib, Owen H Oakley, and Yiannis Constantinides. Fully coupled fluid-structure interaction for offshore applications. In *ASME 2009 28th International Conference on Ocean, Offshore and Arctic Engineering*, pages 757–765. American Society of Mechanical Engineers, 2009.
- [9] Samuel Holmes, Owen H Oakley, and Yiannis Constantinides. Simulation of riser viv using fully three dimensional cfd simulations. In *25th International Conference on Offshore Mechanics and Arctic Engineering*, pages 563–570. American Society of Mechanical Engineers, 2006.
- [10] Kjell Herfjord, SO Drange, and Trond Kvamsdal. Assessment of vortex-induced vibrations on deepwater risers by considering fluid-structure interaction. *Journal of Offshore Mechanics and Arctic Engineering*, 121(4):207–212, 1999.
- [11] Andrew J Lofthouse and Buxton Nathan. Cfd modeling of b-52 and kc-135 in air refueling formation. In *35th AIAA Applied Aerodynamics Conference*, page 4236, 2017.
- [12] Kapseong Ro and James W Kamman. Modeling and simulation of hose-paradrogue aerial refueling systems. *Journal of guidance, control, and dynamics*, 33(1):53–63, 2010.
- [13] ZH Zhu and SA Meguid. Modeling and simulation of aerial refueling by finite element method. *International Journal of Solids and Structures*, 44(24):8057–8073, 2007.
- [14] Andrey Styuart, Robert Gaston, Hisako Yamashiro, Robert Stirling, and Marat Mor. Numerical simulation of hose whip phenomenon in aerial refueling. In *AIAA Atmospheric Flight Mechanics Conference*, page 6211, 2011.
- [15] Yongsam Kim and Charles S Peskin. 2–d parachute simulation by the immersed boundary method. *SIAM Journal on Scientific Computing*, 28(6):2294–2312, 2006.

- [16] Charles S Peskin. Numerical analysis of blood flow in the heart. *Journal of computational physics*, 25(3):220–252, 1977.
- [17] Rajat Mittal and Gianluca Iaccarino. Immersed boundary methods. *Annu. Rev. Fluid Mech.*, 37:239–261, 2005.
- [18] Jung-II Choi, Roshan C Oberoi, Jack R Edwards, and Jacky A Rosati. An immersed boundary method for complex incompressible flows. *Journal of Computational Physics*, 224(2):757–784, 2007.
- [19] Yu-Heng Tseng and Joel H Ferziger. A ghost-cell immersed boundary method for flow in complex geometry. *Journal of computational physics*, 192(2):593–623, 2003.
- [20] Kevin Wang, Arthur Rallu, J-F Gerbeau, and Charbel Farhat. Algorithms for interface treatment and load computation in embedded boundary methods for fluid and fluid–structure interaction problems. *International Journal for Numerical Methods in Fluids*, 67(9):1175–1206, 2011.
- [21] V Lakshminarayan, C Farhat, and A Main. An embedded boundary framework for compressible turbulent flow and fluid–structure computations on structured and unstructured grids. *International Journal for Numerical Methods in Fluids*, 76(6):366–395, 2014.
- [22] Alex Main, Xianyi Zeng, Philip Avery, and Charbel Farhat. An enhanced fiver method for multi-material flow problems with second-order convergence rate. *Journal of Computational Physics*, 329:141–172, 2017.
- [23] Daniel Z Huang, Dante De Santis, and Charbel Farhat. A family of position-and orientation-independent embedded boundary methods for viscous flow and fluid–structure interaction problems. *Journal of Computational Physics*, 365:74–104, 2018.
- [24] Raunak Borker, Daniel Huang, Sebastian Grimberg, Charbel Farhat, Philip Avery, and Jason Rabinovitch. Mesh adaptation framework for embedded boundary methods for computational fluid dynamics and fluid-structure interaction. *International Journal for Numerical Methods in Fluids*, 2019.
- [25] Mayuresh J Patil, Dewey H Hodges, and Carlos E S. Cesnik. Nonlinear aeroelastic analysis of complete aircraft in subsonic flow. *Journal of Aircraft*, 37(5):753–760, 2000.
- [26] Rafael Palacios, Joseba Murua, and Robert Cook. Structural and aerodynamic models in nonlinear flight dynamics of very flexible aircraft. *AIAA journal*, 48(11):2648–2659, 2010.
- [27] David J Malcolm and Daniel L Laird. Modeling of blades as equivalent beams for aeroelastic analysis. In *ASME 2003 Wind Energy Symposium*, pages 293–303. American Society of Mechanical Engineers, 2003.
- [28] Lin Wang, Xiongwei Liu, Nathalie Renevier, Matthew Stables, and George M Hall. Nonlinear aeroelastic modelling for wind turbine blades based on blade element momentum theory and geometrically exact beam theory. *Energy*, 76:487–501, 2014.
- [29] Charbel Farhat, Michael Lesoinne, and Patrick Le Tallec. Load and motion transfer algorithms for fluid/structure interaction problems with non-matching discrete interfaces: Momentum and energy conservation, optimal discretization and application to aeroelasticity. *Computer methods in applied mechanics and engineering*, 157(1-2):95–114, 1998.
- [30] Trond Kvamsdal, Knut M Okstad, Karstein Sørli, and Pierre Pegon. Two-level adaptive mesh movement algorithms for fsi-computations. 1999.
- [31] Charles S Peskin. Flow patterns around heart valves: a numerical method. *Journal of computational physics*, 10(2):252–271, 1972.
- [32] Hans Johansen and Phillip Colella. A cartesian grid embedded boundary method for poisson’s equation on irregular domains. *Journal of Computational Physics*, 147(1):60–85, 1998.

- [33] EA Fadlun, R Verzicco, P. Orlandi, and J Mohd-Yusof. Combined immersed-boundary finite-difference methods for three-dimensional complex flow simulations. *Journal of computational physics*, 161(1):35–60, 2000.
- [34] Jungwoo Kim, Dongjoo Kim, and Haecheon Choi. An immersed-boundary finite-volume method for simulations of flow in complex geometries. *Journal of Computational Physics*, 171(1):132–150, 2001.
- [35] Rainald Löhner, Joseph D Baum, Eric Mestreau, Dmitri Sharov, Charles Charman, and Daniele Pelessone. Adaptive embedded unstructured grid methods. *International Journal for Numerical Methods in Engineering*, 60(3):641–660, 2004.
- [36] HKRM Uddin, RMJ Kramer, and Carlos Pantano. A cartesian-based embedded geometry technique with adaptive high-order finite differences for compressible flow around complex geometries. *Journal of Computational Physics*, 262:379–407, 2014.
- [37] Roland Glowinski, Tsorng-Whay Pan, Anthony J Kearsley, and Jacques Periaux. Numerical simulation and optimal shape for viscous flow by a fictitious domain method. *International Journal for Numerical Methods in Fluids*, 20(8-9):695–711, 1995.
- [38] Michael J Aftosmis, Marsha J Berger, and John E Melton. Robust and efficient cartesian mesh generation for component-based geometry. *AIAA journal*, 36(6):952–960, 1998.
- [39] C Farhat, A Rallu, K Wang, and T Belytschko. Robust and provably second-order explicit–explicit and implicit–explicit staggered time-integrators for highly non-linear compressible fluid–structure interaction problems. *International Journal for Numerical Methods in Engineering*, 84(1):73–107, 2010.
- [40] RMJ Kramer, F Cirak, and C Pantano. Fluid–structure interaction simulations of a tension-cone inflatable aerodynamic decelerator. *AIAA journal*, 2013.
- [41] Cyrill W Hirt, Anthony A Amsden, and JL Cook. An arbitrary lagrangian-eulerian computing method for all flow speeds. *Journal of computational physics*, 14(3):227–253, 1974.
- [42] Jean Donea, S Giuliani, and Jean-Pierre Halleux. An arbitrary lagrangian-eulerian finite element method for transient dynamic fluid-structure interactions. *Computer methods in applied mechanics and engineering*, 33(1-3):689–723, 1982.
- [43] Charbel Farhat, Arthur Rallu, and Sriram Shankaran. A higher-order generalized ghost fluid method for the poor for the three-dimensional two-phase flow computation of underwater implosions. *Journal of Computational Physics*, 227(16):7674–7700, 2008.
- [44] Charbel Farhat and Vinod K Lakshminarayan. An ale formulation of embedded boundary methods for tracking boundary layers in turbulent fluid–structure interaction problems. *Journal of Computational Physics*, 263:53–70, 2014.
- [45] KG Wang, P Lea, and C Farhat. A computational framework for the simulation of high-speed multi-material fluid–structure interaction problems with dynamic fracture. *International Journal for Numerical Methods in Engineering*, 104(7):585–623, 2015.
- [46] Ronald P Fedkiw, Tariq Aslam, Barry Merriman, and Stanley Osher. A non-oscillatory eulerian approach to interfaces in multimaterial flows (the ghost fluid method). *Journal of computational physics*, 152(2):457–492, 1999.
- [47] Rob Stevenson. The completion of locally refined simplicial partitions created by bisection. *Mathematics of computation*, 77(261):227–241, 2008.
- [48] Philippe Spalart and Steven Allmaras. A one-equation turbulence model for aerodynamic flows. In *30th aerospace sciences meeting and exhibit*, page 439, 1992.

- [49] Juan R Cruz, David W Way, Jeremy D Shidner, Jody L Davis, Douglas S Adams, and Devin M Kipp. Reconstruction of the mars science laboratory parachute performance. *Journal of Spacecraft and Rockets*, 51(4):1185–1196, 2014.
- [50] Armen Derkevorkian, Philip Avery, Daniel Z. Huang, Charbel Farhat, Jason Rabinovitch, and Lee Peterson. Effects of structural parameters on the fsi simulation of supersonic parachute deployments. In *AIAA Aviation 2019 Forum*, page 3276, 2019.
- [51] John K Lin, Lauren S Shook, Joanne S Ware, and Joseph V Welch. Flexible material systems testing. 2010.
- [52] AW Vreman. An eddy-viscosity subgrid-scale model for turbulent shear flow: Algebraic theory and applications. *Physics of fluids*, 16(10):3670–3681, 2004.
- [53] William F Mitchell. *Unified multilevel adaptive finite element methods for elliptic problems*. PhD thesis, Citeseer, 1988.
- [54] Carmelo Militello and Carlos A Felippa. The first andes elements: 9-dof plate bending triangles. *Computer Methods in Applied Mechanics and Engineering*, 93(2):217–246, 1991.
- [55] Daniel Z Huang, Man Long Wong, Sanjiva K Lele, and Charbel Farhat. A homogenized flux-body force approach for modeling porous wall boundary conditions in compressible viscous flows. *arXiv preprint arXiv:1907.09632*, 2019.